MHD Boger Dusty Nanofluid Flow: Nanoparticle Aggregation and Esterification Effects over a Stretching Sheet

Muzammil Hussain[a], Aziz Ullah Awan[a,b,*]

[a]Institute of Mathematics, University of the Punjab, Lahore 54590, Pakistan

[b]Center for Theoretical Physics, Khazar University, 41 Mehseti Str., Baku, AZ1096, Azerbaijan

*Corresponding author: aziz.math@pu.edu.pk (Aziz Ullah Awan)

Abstract

This research addresses the challenges of heat transfer optimization in non-Newtonian Boger dusty nanofluid flow across a stretching sheet by investigating the combined effects of viscoelasticity, reversible reactions, magnetohydrodynamics, and buoyancy forces. This study is highly relevant to various engineering problems, particularly in solar energy systems. In such applications, stretched sheet models simulate solar absorber surfaces; dusty nanofluids enhance thermal absorption and conductivity; nanoparticle aggregation affects thermal efficiency and flow stability under solar exposure; and magnetic fields regulate the fluid motion in magnetized environments. The effective thermophysical properties of nanofluids, incorporating aggregation and homogeneous models, are analyzed using the Tiwari-Das model. The non-dimensionalization of the governing partial differential equations is carried out via the similarity technique, and the transformed ordinary differential equations are solved using the shooting method and the Runge-Kutta-Fehlberg (RKF45) technique. The consistency of numerical results is verified through comparison with previously published research for limiting cases. The influence of underlying factors on flow and thermal characteristics is systematically explored through plots. It is observed that aggregated nanoparticles constrict streamlines, diminishing flow speed while improving heat transfer by augmenting temperature and Nusselt number. Dusty nanofluid moves more slowly than pure nanofluid due to higher drag induced by suspended dust particles. The equilibrium constant positively impacts the temperature profile, whereas the velocity and concentration profiles are negatively affected.

Keywords: Boger dusty nanofluid; Nanoparticle aggregation; Stretching sheet; Buoyancy effects; Heat transfer; Esterification process.

1. Introduction

Nanofluids are engineered dispersions of nanoparticles in base fluids, which improve thermal characteristics. Choi and Eastman [1] proposed the idea of incorporating nanoparticles (in the range of 1-100 nm) into conventional fluids such as water, oil, and lubricants to increase thermal conductivity. The rheological and thermal transport characteristics of Casson nanofluid flow through an elongated cylinder were highlighted by Malik et al. [2]. Nanofluid bioconvection was investigated by Ali et al. [3] in the presence of a permeable wedge and a magnetic field. Abbas et al. [4] used the Buongiorno model to investigate the thermodynamic behavior of Sutterby fluids across a nonlinear stretching cylinder. Recent advancements in

nanofluid research, such as new models and applications, have shown the growing significance of nanofluids in advanced thermal management systems [5-10].

The stability and efficiency of nanofluids are greatly impacted by nanoparticle aggregation, which is a clustering of nanoparticles brought on by intermolecular interactions. It affects homogeneity, mechanical strength, and biodistribution in the biological and material sciences; stabilizers and surface alterations aid in controlling aggregation for optimal performance. Nanoparticle aggregation [11,12], nanoparticle movement [13], and nanolayers [14] are cited as important components of nanofluid thermal conductivity. Its function in improving heat transport is confirmed by experiments [14,15]. Kumar et al. [16] examined the nanofluid flow over a porous slider that expands and contracts while considering the role of nanoparticle aggregation. Kezzar et al. [17] used modified Krieger-Dougherty and Maxwell-Bruggeman models to study nanoparticle aggregation in an MHD nanofluid flow. Nanoparticle aggregation and convective effects on nanofluid flow past a coaxial cylinder under thermal radiation were investigated by Albalawi et al. [18].

Dusty fluid flow affects both industrial and natural processes through the suspension of micron-sized solid particles in a fluid. Chemical interactions aid in raindrop formation by promoting the dispersion of tiny particles during the fluidization process. Applications include precision-guidance technology, paint spraying, biomedical systems, and reactor cooling. Using Stokes' drag law, Saffman [19] developed the fundamental equations for dusty fluids, highlighting their implications for enhanced thermal transfer. Dey and Chutia [20] explored the bioconvective flow in dusty nanofluids. Sharif et al. [21] studied the flow of trihybrid Ellis dusty nanofluid across a Riga plate. Hussain et al. [22] analyzed the complex effects of nanoparticle radius on heat transfer driven by natural convection in an MHD dusty nanofluid across a stretched sheet. Naz [23] evaluated the behavior of Brinkman-type magnetized dusty fluid flow inside a penetrable microchannel, driven by injection-suction mechanisms and transient pressure fluctuations.

Boger fluids [24] are a special family of non-Newtonian fluids that show persistent viscosity over a wide range of shear rates. Boger fluids' consistent viscosity and noticeable elastic nature make them ideal for fiber spinning, coating, and polymer processing. Boger fluids are often made with extremely viscous solvents to counteract the significant shear-thinning effects caused by the addition of polymers. Ali et al. [25] investigated the impact of Lorentz and Coriolis forces on spinning Boger nanofluid using the finite element method. Subsequently, Ali et al. [26] explored the magnetized squeezing flow of Boger micropolar nanofluid confined between two parallel disks. Abbas et al. [27] numerically evaluated chemically reactive Boger fluid flow past a heated sheet, accounting for local thermal nonequilibrium (LTNE) effects. Okasha et al. [28] looked into the elastic distortion in Boger hybrid nanofluid flow past a plate, considering LTNE and relaxation times for mass and heat transmission.

A meticulous review of the published literature uncovers a significant research gap: the integrated effects of buoyancy forces, nanoparticle aggregation, viscoelasticity, magnetohydrodynamics, and esterification in the context of non-Newtonian Boger dusty nanofluid flow over a stretching sheet have not been examined. This flow configuration is critical because it is used in industries such as polymer processing, surface coating, and glass fiber production, where managing non-Newtonian fluid behavior has a direct impact on product uniformity and thermal quality. The fluid examined in this study is a multiphase medium

composed of (i) a Boger viscoelastic base fluid, (ii) homogeneously dispersed copper (Cu) nanoparticles, and (iii) micron-scale dust particles. Boger fluids, formed by adding a small amount of high-molecular-weight polymer to a Newtonian solvent, exhibit linear elastic behavior and constant viscosity, making them ideal for isolating elastic effects without shear-thinning interference. Because of their ability to retain elastic energy during deformation, these materials are frequently used in simulating practical polymeric systems. Dusty flows are pertinent to environmental applications like pollution control and filtration. Nanoparticle clustering, caused by van der Waals and electrostatic interactions, influences heat transmission and flow dynamics, but it is rarely explored in viscoelastic multiphase environments. The inclusion of a reversible esterification mechanism increases industrial significance due to its importance in the production of biofuels, pharmaceuticals, polymers, and fine chemicals. The coupled effects of these flow phenomena remain understudied; this work addresses them to fill the research gap. A comparison with previous research is given below to emphasize the uniqueness of this effort. Table 1 summarizes recent literature and clearly shows that no prior study has concurrently addressed all the aspects considered in this work.

The current investigation presents the following key contributions:

- Development of a novel model for magnetohydrodynamic Boger dusty nanofluid flow over a stretching sheet.
- Implementation of the Tiwari-Das model to investigate the thermal characteristics of dusty nanofluid flow.
- Exploration of mixed convection and magnetic field interactions with viscoelastic and dusty effects.
- Assessment of nanoparticle aggregation's impact on thermophysical properties and evaluation of its role in optimizing thermal performance.
- Coupling of reversible chemical reaction kinetics with solute transport in a multiphase medium.

2. Flow analysis

2.1 Problem description

This article delves into the steady, incompressible magnetohydrodynamic (MHD) flow of a Boger dusty nanofluid past a linearly stretching surface. The paper introduces the dust phase using a two-fluid model, in which the dust and nanofluid serve as interpenetrating continua. Unlike conventional single-phase nanofluid models, the dusty nanofluid formulation allows the simulation of velocity lag, thermal lag, and interphase momentum exchange. These effects are significant in systems containing suspended particles.

The primary goal of enhancing heat transfer is achieved by the inclusion of nanoparticles, which are chosen as copper due to their excellent thermal conductivity. These particles are assumed to be monodispersed, spherical, and isotropic. Their presence significantly alters the

density, viscosity, thermal conductivity, and specific heat of the nanofluid. The Tiwari-Das model is adopted to characterize the effective thermophysical properties, while nanoparticle aggregation is accounted for via modified Krieger–Dougherty and Maxwell–Bruggeman models. The dust phase is modeled as uniformly distributed spherical particles that interact with the fluid phase through Stokes drag. The existence of nanoparticles and dust particles corresponds to real-world multiphase industrial processes such as paper coating, solar energy harvesting, and inkjet printing. The assumption of a no-slip condition between the fluid and dust phases implies strong coupling. In moderate flow patterns with negligible particle inertia, this assumption is valid. However, slip effects might become non-negligible in industries with strong shear or high inertia (like polymer extrusion), which could have an impact on thermal transport and momentum.

The $\tilde{x}$-axis lies along the surface, whereas the $\tilde{y}$-axis extends normally outward. The surface stretches with velocity $u_{1w}(\tilde{x}) = a\tilde{x}$, where the constant $a > 0$ is stretching rate. A constant transverse magnetic field B_0 is oriented normal to the stretching sheet, introducing Lorentz forces that resist fluid flow. Hall current effects and Ohmic dissipation are neglected due to the relatively small magnetic field strength [33]. Thermal and solutal gradients are imposed at the sheet surface, characterized by wall temperature T_w and wall solute concentration C_w^*, while the corresponding ambient values are T_∞ and C_∞^*, respectively. Figure 1 schematically illustrates the physical flow configuration. The study takes into account both aggregated and non-aggregated nanoparticle cases to determine their effect on fluid flow and heat transfer. Under the presumptions of modest internal heat generation and mild velocity gradients, which are generally true for classical boundary layer flows, viscous dissipation is not included in the energy equation.

2.2 Governing equations

Boger fluids are idealized non-Newtonian fluids with constant shear viscosity and a nonzero elastic modulus, meaning that they resist deformation through elastic recoil. Boger fluids are carefully engineered to exhibit elastic behavior while keeping constant viscosity, typically by adding a small concentration of flexible polymer to a viscous Newtonian fluid. Mathematically, the viscoelastic behavior of Boger fluid is captured by the dimensionless parameters Λ_1 and Λ_2, which appear in the momentum equation. Here, Λ_1 represents the solvent fraction parameter, quantifying the relative influence of Newtonian solvent in the fluid mixture. The parameter Λ_2 denotes the relaxation time ratio, which introduces the fluid's viscoelasticity. It is the ratio of elastic relaxation time to the characteristic flow time scale. The modified stress term $\frac{1+\Lambda_1}{1+\Lambda_2}$ incorporates the Boger fluids' fundamental non-Newtonian effects. Based on the assumptions, the equations governing the flow are as follows [27, 30, 34, 35]:

$$\frac{\partial u_1}{\partial \tilde{x}} + \frac{\partial u_2}{\partial \tilde{y}} = 0, \tag{1}$$

$$u_1\frac{\partial u_1}{\partial \tilde{x}}+u_2\frac{\partial u_1}{\partial \tilde{y}}=\nu_{nf}\left(\frac{1+\Lambda_1}{1+\Lambda_2}\right)\frac{\partial^2 u_1}{\partial \tilde{y}^2}+\frac{KN}{\rho_{nf}}(u_{1p}-u_1)-\frac{\sigma_{nf}B_0^2}{\rho_{nf}}u_1 \tag{2}$$

$$+\frac{\tilde{g}_1}{\rho_{nf}}\left[\tilde{\beta}(T-T_\infty)\rho_f(1-C_\infty^*)+(C^*-C_\infty^*)(\rho_f-\rho_p)\right]$$

$$(\rho c_p)_{nf}\left[u_1\frac{\partial T}{\partial \tilde{x}}+u_2\frac{\partial T}{\partial \tilde{y}}\right]=k_{nf}\frac{\partial^2 T}{\partial \tilde{y}^2}+\frac{(c_p)_f\rho_p}{\tau_T}(T_p-T), \tag{3}$$

$$u_1\frac{\partial C^*}{\partial \tilde{x}}+u_2\frac{\partial C^*}{\partial \tilde{y}}=D_B\frac{\partial^2 C^*}{\partial \tilde{y}^2}-\frac{\rho_p}{\rho\tau_C}(C_-^*C_p^*), \tag{4}$$

for the dust phase

$$\frac{\partial u_{1p}}{\partial \tilde{x}}+\frac{\partial u_{2p}}{\partial \tilde{y}}=0, \tag{5}$$

$$u_{1p}\frac{\partial u_{1p}}{\partial \tilde{x}}+u_{2p}\frac{\partial u_{1p}}{\partial \tilde{y}}=\frac{K}{m}(u_1-u_{1p}), \tag{6}$$

$$u_{1p}\frac{\partial T_p}{\partial \tilde{x}}+u_{2p}\frac{\partial T_p}{\partial \tilde{y}}=\frac{c_p}{\tau_T c_m}(T-T_p), \tag{7}$$

$$u_{1p}\frac{\partial C_p^*}{\partial \tilde{x}}+u_{2p}\frac{\partial C_p^*}{\partial \tilde{y}}=\frac{Nm}{\tau_c\rho}(C^*-C_p^*), \tag{8}$$

where (u_1,u_2) denote the velocity components of the nanofluid phase along the sheet and normal to the sheet, respectively; likewise, (u_{1p},u_{2p}) are the corresponding dust phase velocity components. The temperatures and concentrations of fluid and dust phases are denoted as (T,T_p) and (C^*,C_p^*), respectively. The terms k_{nf}, σ_{nf}, $(c_p)_{nf}$, ν_{nf}, and ρ_{nf} indicate the thermal conductivity, electrical conductivity, heat capacity, kinematic viscosity, and density of the nanofluid, respectively. The term ρ_p is the density of dust particles, D_B is Brownian diffusion, and $\tilde{g}_1$ shows gravitational acceleration. The terms m, N, τ_T, c_m, and K denote dust particle mass, dust particle concentration, thermal relaxation time, dust particle specific heat capacity, and Stokes' drag constant, respectively.

2.3 Diffusive behavior of solute

The solute is present in the following two distinct forms during the esterification process:

- Freely diffused solute C^*, representing unreacted species.
- Reacted solute C^{**}, localized at the reaction point.

To incorporate the esterification process into the model, it is considered as a reversible second-order reaction governed by an equilibrium constant K_{eq}, which relates the rates of ester formation to the rate of hydrolysis. It links the reacted solute concentration C^{**} with the unreacted solute concentration C^*. Under the assumption of local chemical equilibrium and fast reaction kinetics relative to diffusion, the concentrations of the two forms are connected by:

$$C^{**} = K_{\text{eq}} C^*. \tag{9}$$

The general mass balance equation over a control volume $A\Delta y$ is given as follows [29,30]:

(accumulation in $A\Delta y$) = (diffusive inflow minus diffusive outflow)

+(production from reaction in $A\Delta y$). (10)

Accordingly, the diffusing solute's mass balance can be written as:

$$u_1 \frac{\partial C^*}{\partial \tilde{x}} + u_2 \frac{\partial C^*}{\partial \tilde{y}} = D_B \frac{\partial^2 C^*}{\partial \tilde{y}^2} - \frac{\rho_p}{\rho \tau_C} (C^* - C_p^*) + \tilde{r}_1, \tag{11}$$

where the reversible chemical reaction rate is represented by $\tilde{r}_1$. For the reacted solute, which is assumed to be non-diffusing, the mass balance is articulated as:

$$u_1 \frac{\partial C^{**}}{\partial \tilde{x}} + u_2 \frac{\partial C^{**}}{\partial \tilde{y}} = -\tilde{r}_1. \tag{12}$$

The reaction term $\tilde{r}_1$ appears with the same magnitude but opposite sign, reflecting the transformation of C^* into C^{**}. Adding Eqs.(11) and (12) eliminates $\tilde{r}_1$.

$$u_1 \frac{\partial}{\partial \tilde{x}}(C^* + C^{**}) + u_2 \frac{\partial}{\partial \tilde{y}}(C^* + C^{**}) = D_B \frac{\partial^2 C^*}{\partial \tilde{y}^2} - \frac{\rho_p}{\rho \tau_C}(C^* - C_p^*), \tag{13}$$

substituting the equilibrium condition $C^{**} = K_{\text{eq}} C^*$, we obtain:

$$u_1 \frac{\partial C^*}{\partial \tilde{x}} + u_2 \frac{\partial C^*}{\partial \tilde{y}} = \frac{D_B}{1+K_{\text{eq}}} \frac{\partial^2 C^*}{\partial \tilde{y}^2} - \frac{1}{1+K_{\text{eq}}} \frac{\rho_p}{\rho \tau_C}(C^* - C_p^*). \tag{14}$$

The impact of esterification appears as a scaling factor $\frac{1}{1+K_{\text{eq}}}$, which reduces the effective diffusion and interphase mass transfer due to the conversion of solute into product. The equilibrium constant K_{eq} is defined as:

$$K_{\text{eq}} = \frac{[\text{Ester}][\text{Water}]}{[\text{Alcohol}][\text{Acid}]}. \tag{15}$$

The equilibrium constant K_{eq} is temperature-dependent, although it is assumed to be steady in our study due to moderate thermal change within the boundary layer. K_{eq} obeys the van't Hoff relation, meaning that, depending on the reaction's enthalpy change, raising the temperature can cause the equilibrium to shift toward either the product or the reactant. Higher temperatures help to decrease the equilibrium constant, favoring hydrolysis in esterification, which is normally exothermic. Nonetheless, the wall temperature is preset, and temperature fluctuations stay within a small range in boundary layer flows across a stretching surface. Therefore, it is not anticipated that the local equilibrium assumption employed to represent the reversible process will be significantly affected by the influence of temperature on K_{eq}. This is a common simplification in esterification processes in the flow over a stretching sheet.

2.4 Boundary conditions

The following boundary conditions are provided to represent the behavior of the dust and nanofluid phases in the far field and close to the stretching surface [22,34]:

$$\begin{cases} u_1 = u_{1w}(\tilde{x}) = a\tilde{x}, \quad u_2 = 0, \quad T = T_w, \quad C^* = C_w^*, \quad \text{for} \quad \tilde{y} = 0, \\ u_1 \to 0, u_{1p} \to 0, u_{2p} = u_2 \to 0, T \to T_\infty, T_p \to T_\infty, C^* \to C_\infty^*, C_p^* \to C_\infty^*, \text{for} \quad \tilde{y} \to \infty. \end{cases} \tag{16}$$

The stated boundary conditions delineate the boundary layer flow of an MHD Boger dusty nanofluid across a linearly stretched sheet. At the sheet ($\tilde{y} = 0$), tangential velocity condition $u_1 = a\tilde{x}$ reflects the sheet's linear stretching, simulating industrial applications such as

melt-spinning and polymer extrusion. The condition $(u_2 = 0)$ ensures no penetration. Wall temperature and concentration boundary conditions $(T = T_w, C^* = C_w^*)$ denote temperature and concentration at the surface. Far away from the sheet $(\tilde{y} \to \infty)$, all velocity components decay to zero, showing that the fluid is at rest outside the boundary layer. Simultaneously, solute concentration and temperature profiles asymptotically tend to their ambient conditions $(T \to T_\infty, T_p \to T_\infty, C^* \to C_\infty^*, C_p^* \to C_\infty^*)$, guaranteeing stability under equilibrium conditions at infinity. Collectively, these boundary conditions effectively describe the boundary layer flow of dusty nanofluid across a stretched sheet.

2.5 Thermophysical properties

The Tiwari-Das model is used in this study to examine the thermophysical characteristics of the nanofluid, specifically the augmentation of heat transfer caused by suspended nanoparticles. The nanofluid is viewed as a continuum in this single-phase model, with altered effective characteristics (specific heat, density, viscosity, and thermal conductivity) that depend on the volume fraction of nanoparticles.

Nanoparticle aggregation is incorporated into the model by modifying the effective volume fraction Φ_{agr}, which accounts for the tendency of individual nanoparticles to cluster due to interparticle forces such as steric effects, van der Waals attraction, and electrostatic interactions. This aggregated state significantly alters the stability, rheology, and performance of nanofluids by changing their thermophysical properties. These modified properties are reflected in the thermal diffusivity, density, viscosity, and specific heat terms used in the momentum and energy equations. As a result, aggregation modifies temperature and velocity distributions by altering heat transfer and momentum diffusion inside the boundary layer. In engineering applications, uncontrolled aggregation can cause sedimentation, performance reduction, and clogging, whereas carefully planned surface modification and stabilizing agents can help mitigate these effects [36]. Understanding the mechanisms of aggregation is required to improve nanoparticle dispersion and achieve the desired efficiency in a variety of applications, such as drug delivery systems, diagnostic imaging, targeted cancer therapy, and thermal management systems in electronics. Table 2 summarizes nanofluid's thermophysical characteristics with and without nanoparticle aggregation as [37-39]:

The subscripts *agr*, *f*, and *s* refer to aggregated nanoparticles, base fluid, and solid nanoparticles. Φ, Φ_{agr}, and Φ_{max} denote nanoparticle volume fraction, effective volume fraction of aggregates, and maximum particle packing fraction, respectively. The effective aggregate volume fraction, Φ_{agr}, is a nonlinear function of primary nanoparticle volume fraction, Φ. Unlike Φ, which only considers isolated uniformly dispersed nanoparticles, Φ_{agr} accounts for spatial expansion due to particle clustering. Its formulation incorporates the impacts of inter-particle forces and aggregate geometry. It represents the volumetric contribution made by fractal-like aggregates instead of isolated particles. Φ_{agr} more accurately describes the impact of nanoparticle aggregation on viscosity augmentation and thermal conductivity modification than Φ alone.

2.6 Transformations

Similarity transformations used to convert the governing PDEs into ODEs are given below [22,34]:

$$\begin{cases} u_1 = af'(\eta)\tilde{x},\ \eta = \left(\dfrac{a}{\nu_f}\right)^{0.5} y,\ u_2 = -f(\eta)\left(a\nu_f\right)^{0.5},\ u_{2p} = -f_p(\eta)\left(a\nu_f\right)^{0.5},\ \theta(\eta)\left(T_w - T_\infty\right) = T - T_\infty, \\ \theta_p(\eta)\left(T_w - T_\infty\right) = T_p - T_\infty, \phi(\eta)\left(C_w^* - C_\infty^*\right) = C^* - C_\infty^*,\ u_{1p} = af_p'(\eta)\tilde{x},\ \phi_p(\eta)\left(C_w^* - C_\infty^*\right) = C_p^* - C_\infty^*. \end{cases} \tag{17}$$

Here, η is the dimensionless similarity variable, $f(\eta)$ and $f_p(\eta)$ are the stream functions representing the fluid and dust phase velocities, $\theta(\eta)$, $\theta_p(\eta)$ are the dimensionless temperature profiles, and $\phi(\eta)$, $\phi_p(\eta)$ denote solute concentration profiles for the respective phases. These transformations are derived under the boundary layer assumptions of steady, two-dimensional, incompressible flow over a linearly stretching surface, with constant fluid properties and negligible pressure gradients. The similarity approach simplifies the problem by collapsing spatial variables into a single independent variable, enabling the transformation of coupled PDEs into ODEs for efficient numerical analysis.

2.7 Dimensionless system

By applying the transformations given in Eq. (17), Eqs.(1) and (5) are automatically satisfied. The remaining governing equations take the following form:

$$\frac{\alpha_1}{\alpha_2}\left(\frac{1+\Lambda_1}{1+\Lambda_2}\right) f''' - f'^2 + ff'' + \frac{\Gamma_v \beta_v}{\alpha_2}\left(f_p' - f'\right) - \frac{\alpha_3}{\alpha_2} M f' + \frac{\lambda_\theta}{\alpha_2}(\theta - N_r\phi) = 0, \tag{18}$$

$$\frac{\alpha_4}{\alpha_5}\theta'' + Prf\theta' = \frac{\gamma_t Pr\beta_t}{\alpha_5}\left(\theta - \theta_p\right), \tag{19}$$

$$\phi'' + S_c(1+K_{\text{eq}})f\phi' = S_c\beta_c\Gamma_v\left(\phi - \phi_p\right), \tag{20}$$

$$f_p f_p'' = f_p'^2 - \beta_v(f_p' - f'), \tag{21}$$

$$\theta_p' = \frac{\gamma_t\beta_t}{f_p}\left(\theta_p - \theta\right), \tag{22}$$

$$\phi_p' = \frac{\Gamma_v \beta_c}{f_p}\left(\phi_p - \phi\right). \tag{23}$$

These equations incorporate the buoyancy parameters (N_r, λ_θ), Prandtl number Pr, magnetic parameter M, Schmidt number S_c, and dusty fluid parameters $(\gamma_t, \Gamma_v, \beta_t, \beta_c, \beta_v)$. The dimensionless parameters are defined as:

$$\begin{cases} \beta_v = \left(a\tau_v\right)^{-1}, M = \dfrac{B_0^2 \sigma_f}{a\rho_f}, \dfrac{k_{nf}}{k_f} = \alpha_4, Pr = \dfrac{\mu_f (c_p)_f}{k_f}, \\ \dfrac{\mu_{nf}}{\mu_f} = \alpha_1, \gamma_t = \dfrac{c_p}{c_m}, S_c = \dfrac{\nu_f}{D_B}, \lambda_\theta = \dfrac{(T_w - T_\infty)\tilde{\beta}\tilde{g}_1(1-C_\infty^*)}{au_{1w}}, \\ \Gamma_v = \dfrac{Nm}{\rho}, \ \beta_c = \left(a\tau_c\right)^{-1}, \ \dfrac{(\rho c_p)_{nf}}{(\rho c_p)_s} = \alpha_5, \ \dfrac{\sigma_{nf}}{\sigma_f} = \alpha_3, \\ N_r = \dfrac{(\rho_p - \rho_f)(C_w^* - C_\infty^*)}{\tilde{\beta}^* \rho_f (1-C_\infty^*)(T_w - T_\infty)}, \quad \dfrac{\rho_{nf}}{\rho_s} = \alpha_2, \quad \beta_t = \left(a\tau_t\right)^{-1}. \end{cases} \tag{24}$$

Table 3 gives the physical interpretation of key physical parameters used in this study.

the boundary constraints (16) are reduced as:

$$\begin{cases} f(\eta) = 0, \ f'(\eta) = 1, \ \theta(\eta) = \phi(\eta) = 1, \ \text{when } \eta = 0, \\ f_p'(\eta) \to 0, \ f'(\eta) \to 0, \ f_p(\eta) = f(\eta) \to 0, \ \theta_p(\eta) \to 0, \ \theta(\eta) \to 0, \ \phi(\eta) \to 0, \ \phi_p(\eta) \to 0, \quad \text{when } \eta \to \infty. \end{cases} \tag{25}$$

2.8 Engineering quantities

Skin friction factor C_{f_x}, Sherwood number Sh_x, and Nusselt number Nu_x are defined below [40]:

$$C_{f_x} = \frac{\tilde{\tau}_w}{\rho_f u_{1w}^2}, \quad Sh_x = \frac{\tilde{x}\tilde{q}_m}{D_B(C_w^* - C_\infty^*)}, \quad Nu_x = \frac{\tilde{x}\tilde{q}_w}{(T_w - T_\infty)k_f}, \tag{26}$$

Here $\tilde{\tau}_w$, $\tilde{q}_w$, and $\tilde{q}_m$ represent surface shear stress, surface heat flux, and surface mass flux, respectively.

$$\tilde{\tau}_w = \mu_{nf}\left(\frac{1+\Lambda_1}{1+\Lambda_2}\right)\left.\frac{\partial u_1}{\partial \tilde{y}}\right|_{y=0}, \quad \tilde{q}_w = -k_{nf}\left.\frac{\partial T}{\partial \tilde{y}}\right|_{y=0}, \quad \tilde{q}_m = -D_B\left.\frac{\partial C^*}{\partial \tilde{y}}\right|_{y=0}, \tag{27}$$

by using Eqs. (17) and (27) in Eq.(26), the obtained dimensionless form is

$$Cf_x Re_x^{0.5} = \alpha_1\left(\frac{1+\Lambda_1}{1+\Lambda_2}\right) f''(0),\ Nu_x Re_x^{-0.5} = -\alpha_4\theta'(0),\ Sh_x Re_x^{-0.5} = -\phi'(0). \tag{28}$$

Here, $Re_x = \dfrac{a\tilde{x}^2}{\nu_f}$ signifies the local Reynolds number.

3. Chemical background

The esterification process considered in this study is a reversible, second-order chemical reaction that occurs within the solutal boundary layer and significantly changes the distribution of solute species. It involves the reaction of a solute (often alcohol) with a carboxylic acid to produce an ester and water. The equilibrium constant K_{eq} governs this reaction, which occurs concurrently in both the forward (ester formation) and reverse (hydrolysis) directions. It measures the ratio of ester production to hydrolysis at equilibrium and is crucial for modeling chemical conversion occurring in the boundary layer. The reaction is represented as:

$$\text{Acid} + \text{Alcohol} \rightleftharpoons \text{Ester} + \text{Water},$$

with the equilibrium condition given in Eq. (15).

This chemical process is incorporated into the mathematical model using the solute transport equation. The empirically measured K_{eq}, which is utilized to correlate the concentrations of alcohol, acid, and ester, is applied under the assumption of local equilibrium between reacted C^{**} and unreacted C^* solutes. This esterification is coupled to the species concentration equation by a nonlinear source term, which modifies the local solutal gradients. The equilibrium constant K_{eq} is integrated into the solute transport model to represent the equilibrium between the unreacted and reacted solute species, and it is essential in establishing the extent of conversion inside the boundary layer. Any variation in concentration distribution brought on by a chemical reaction immediately affects the momentum equation, which in turn affects the velocity profile, as solutal buoyancy is modeled using the buoyancy ratio parameter N_r. Moreover, the mass transfer parameter S_c, which varies by alcohol type, connects chemical kinetics to boundary layer transport behavior. The esterification process indirectly impacts the dispersion of nanoparticles, thermal profiles, and interfacial transport processes via this coupling.

Accurate determination of K_{eq} is crucial and can be achieved through diverse experimental methodologies, encompassing spectroscopy, polarimetry, and thermochemical analysis. Sarlo et al. [41] conducted a comprehensive investigation to determine K_{eq} values for esterification between ethanoic acid and various alcohols, catalyzed by concentrated sulfuric acid H_2SO_4. The chemical reactions with corresponding experimental values are reported as:

$$CH_3OH + CH_3CO_2H \underset{K_{eq}=5.03}{\rightleftharpoons} CH_3COOCH_3 + H_2O$$

$$C_2H_5OH + CH_3CO_2H \underset{K_{eq}=4.86}{\rightleftharpoons} CH_3CO_2C_2H_5 + H_2O$$

$$C_3H_7OH + CH_3CO_2H \underset{K_{eq}=4.21}{\rightleftharpoons} CH_3CO_2C_3H_7 + H_2O$$

$$C_4H_9OH + CH_3CO_2H \underset{K_{eq}=2.85}{\rightleftharpoons} CH_3CO_2C_4H_9 + H_2O$$

Acetic acid esterification with methanol, ethanol, propanol, and butanol exhibits a clear trend in equilibrium behavior, with K_{eq} values of 5.03, 4.86, 4.21, and 2.85, respectively. The higher equilibrium constant for methanol indicates increased reversibility and product yield, whereas the lower K_{eq} for butanol suggests limited conversion and a shift toward irreversibility. These findings highlight the pivotal role of equilibrium in determining reaction efficiency and justify the use of the fully irreversible case $K_{eq} = 0$ to assess flow behavior under constrained conversion. Investigating these reactions reveals how molecular structure affects equilibrium behavior, which is critical for optimizing reaction conditions in industrial ester synthesis and flow modeling.

4. Solution procedure

The highly nonlinear nature of the resulting ODEs makes obtaining exact solutions extremely challenging, requiring a numerical technique. The Runge-Kutta-Fehlberg (RKF45) method is used to numerically solve the non-dimensional form of nonlinear system (18–23), along with boundary conditions (25). The RKF45 approach is well-suited for initial value problems arising from similarity-transformed multivariate governing equations. In addition to being extremely accurate, this approach eliminates the requirement for domain-wide discretization, which would render finite difference or finite element approaches more computationally expensive. Its adaptive step-size control improves numerical stability and precision, especially for stiff and sensitive flow systems like the current chemically reactive viscoelastic dusty nanofluid model. Unlike fixed-step approaches, RKF45 automatically adapts the step size based on local error estimation, maximizing computational efficiency while maintaining precision. RKF45 does not require splitting the entire domain or generating massive matrices, as finite element or finite difference approaches do. Because of this, it works well with semi-infinite domains, which are frequently found in boundary layer problems that are similarity-transformed. RKF45 effectively resolves the boundary value problem by converting it into an initial value problem (IVP) when used in conjunction with the shooting approach.

To facilitate numerical integration, the system of nonlinear ODEs is restructured into an equivalent system of first-order ODEs by introducing the following substitutions:

$$f = \hat{x}_1, \quad f' = \hat{x}_2, \quad f'' = \hat{x}_3, \quad \theta = \hat{x}_4, \quad \theta' = \hat{x}_5, \quad \phi = \hat{x}_6,$$
$$\phi' = \hat{x}_7, \quad f_p = \hat{x}_8 \quad f_p' = \hat{x}_9, \quad \theta_p = \hat{x}_{10}, \quad \phi_p = \hat{x}_{11},$$

Thus nonlinear system of ODEs is reduced to a system of first-order ODEs.

$$\hat{x}_1' = \hat{x}_2, \tag{29}$$

$$\hat{x}_2' = \hat{x}_3, \tag{30}$$

$$\hat{x}_3' = \frac{\alpha_2}{\alpha_1}\left(\frac{1+\Lambda_2}{1+\Lambda_1}\right)\left[\hat{x}_2^2 - \hat{x}_1\hat{x}_3 - \frac{\Gamma_v\beta_v}{\alpha_2}\left(\hat{x}_9 - \hat{x}_2\right) + \frac{\alpha_3}{\alpha_2}M\hat{x}_2 - \frac{\lambda_\theta}{\alpha_2}\left(\hat{x}_4 - N_r\hat{x}_6\right)\right], \tag{31}$$

$$\hat{x}_4' = \hat{x}_5, \tag{32}$$

$$\hat{x}_5' = \frac{\gamma_t Pr\beta_t}{\alpha_4}\left(\hat{x}_4 - \hat{x}_{10}\right) - \frac{\alpha_5 Pr}{\alpha_4}\hat{x}_1\hat{x}_5, \tag{33}$$

$$\hat{x}_6' = \hat{x}_7, \tag{34}$$

$$\hat{x}_7' = S_c\beta_c\Gamma_v\left(\hat{x}_6 - \hat{x}_{11}\right) - S_c(1+K_{\text{eq}})\hat{x}_1\hat{x}_7, \tag{35}$$

$$\hat{x}_8' = \hat{x}_9, \tag{36}$$

$$\hat{x}_9' = \frac{1}{\hat{x}_8}\left[\hat{x}_9^2 - \beta_v\left(\hat{x}_9 - \hat{x}_2\right)\right], \tag{37}$$

$$\hat{x}_{10}' = \frac{\gamma_t\beta_t}{\hat{x}_8}\left(\hat{x}_{10} - \hat{x}_4\right), \tag{38}$$

$$\hat{x}_{11}' = \frac{\Gamma_v\beta_c}{\hat{x}_8}\left(\hat{x}_{11} - \hat{x}_6\right). \tag{39}$$

With the initial conditions:

$$\begin{cases} \hat{x}_1(0)=0, \quad \hat{x}_2(0)=1, \quad \hat{x}_3(0)=\delta_1, \quad \hat{x}_4(0)=1, \quad \hat{x}_5(0)=\delta_2, \quad \hat{x}_6(0)=1, \\ \hat{x}_7(0)=\delta_3, \quad \hat{x}_8(0)=\delta_4, \quad \hat{x}_9(0)=\delta_5, \quad \hat{x}_{10}(0)=\delta_6, \quad \hat{x}_{11}(0)=\delta_7. \end{cases} \tag{40}$$

The shooting method is used to guess missing initial conditions by an iterative process until the boundary conditions are satisfied. Thus, we require the values for unknowns which are not specified in the boundary conditions. Therefore, we make suitable initial guesses for them. These guesses are selected such that known ambient conditions are satisfied asymptotically. A step size of 0.001 is adopted, and accuracy up to sixth-decimal place is used as the convergence criterion in this study. The model was solved with step sizes of 0.01, 0.005, 0.001, and 0.0005 to verify numerical convergence. The disparities between step sizes 0.001 and 0.0005 were found to be less than 10^{-6}. It demonstrates that the chosen step size is accurate. Furthermore, there was no discernible change in boundary layer profiles throughout this range, indicating that the computational solution is reliable and unaffected by slight adjustments to step size.

5. Numerical validation

Since our study is purely theoretical and, to the best of our knowledge, no experimental research exists on Boger dusty nanofluids involving esterification and nanoparticle aggregation, experimental validation is not feasible. However, under specific limiting cases, our model was checked against existing theoretical results to ensure its reliability. Table 4 compares the present results of skin friction with those reported by Ramesh et al. [42], Jalil et al. [43], and Hussain et al. [22]. All of these works investigated magnetohydrodynamic dusty fluid flow over a stretching sheet. When viscoelasticity, buoyancy, and nanoparticle aggregation are neglected, the current formulation's momentum equation reduces to that of Hussain et al. [22], who studied MHD dusty nanofluid flow without these effects. Further omitting nanoparticles and their thermophysical properties recovers the model of Jalil et al. [43], which provides an exact solution for MHD dusty fluid flow on a flat stretched sheet. Additionally, assuming the impacts of a uniform heat source/sink and aligned sheet yield the momentum structure proposed by Ramesh et al. [42] for MHD dusty fluid flow. Thus, the validity and consistency of the current momentum formulation in forecasting wall shear stress are confirmed.

Similarly, Table 5 provides a comparison of the Nusselt number with the results reported by Wang [44], Khan and Pop [45], and Hussain et al. [31]. All of them focused on the heat transfer past a stretching sheet. The energy equation in the current model is structurally consistent with the Hussain et al. [31] formulation. The present work, however, does not use the Buongiorno model, which means that thermophoresis and Brownian motion are not included in the basic formulation, unlike their study. The Buongiorno model, a traditional nanofluid framework, was also used by Khan and Pop [45], although they did not consider dust particles or the thermophysical properties of nanoparticles into consideration. Moreover, our energy equation simplifies to Wang's traditional thermal boundary layer formulation [44] when neither dust nor nanoparticles are present. The results show great agreement in every case, proving the accuracy

and dependability of the numerical technique used in this investigation. These analogies offer solid theoretical support for the current model's validity.

6. Results and discussion

This section is dedicated to interpreting the impact of physical parameters on the flow and heat transfer characteristics of MHD Boger dusty nanofluid. The default parameter values used in this study are: $\beta_t = 1.0, Pr = 6.2, \Gamma_v = 0.1, \beta_v = 1.0, \gamma_t = 0.1, M = 2.0, S_c = 1.3, N_r = 0.2, \Lambda_1 = 1.0, \Lambda_2 = 2.0, K_{eq} = 4.86,$ and $\lambda_\theta = 1.0$. The effects of these factors on velocity, temperature, and concentration profiles are examined, along with analyses of skin friction and Nusselt number under different parameters.

The impact of the solvent fraction parameter Λ_1 and the relaxation time ratio Λ_2 on the velocity and temperature profiles of both the nanofluid and dust phases is illustrated in Figs. 2 and 3. Increasing the solvent fraction parameter enhances the velocity and temperature profiles for both phases, as shown in Fig. 2a and Fig. 3a. Physically, a larger Λ_1 implies reduced polymer dominance and attenuated elastic effects, making the Boger fluid behave more like a Newtonian fluid. This decline in elasticity diminishes the internal resistance, facilitating greater momentum transfer and resulting in elevated velocity profiles $f'(\eta)$ and $f_p'(\eta)$. Furthermore, the solvent fraction parameter enhances thermal conductivity and improves interphase heat exchange, leading to more efficient thermal transmission and enhanced temperature profiles $\theta(\eta)$ and $\theta_p(\eta)$. Conversely, an augmentation in Λ_2, which characterizes elastic memory, decreases fluid flow due to increased viscoelastic resistance. Figure 2b shows that Λ_2 diminishes the velocity profiles, while Fig. 3b illustrates opposite trends for temperature profiles. As Λ_2 increases, elastic resistance intensifies, reducing fluid motion and velocity profiles. It allows for extended heat exchange, improving heat transfer between the fluid and dust phases. The amplified elastic stresses enhance internal molecular interactions, thereby increasing thermal conductivity and thickening the thermal boundary layer.

Figure 4 illustrates how the magnetic parameter M influences the velocity and temperature profiles for both phases.The application of a magnetic field induces a resistive Lorentz force that impedes fluid motion, decreasing both nanofluid and dust phase velocities. This magnetic damping increases frictional effects while decreasing momentum transfer. Temperature profiles rise as a result of improved heat accumulation and thermal boundary layer expansion. MHD-based magnetic fluid sensors are well-suited for precision sensing, healthcare, and military applications because of their excellent stability, accuracy, and temperature resilience [46,47]. The influence of equilibrium constant K_{eq}, which controls the equilibrium of the esterification reaction, on velocities $(f'(\eta), f_{p'}(\eta))$, temperature $\theta(\eta)$, and concentration $\phi(\eta)$ is outlined in Fig. 5. As seen in Fig. 5a, increasing the equilibrium constant decreases the available solute for diffusion, weakening the concentration gradient and resulting in lower velocities for both phases. Figure 5b demonstrates that stronger reversible reactions enhance mass transport, leading to a thinner concentration boundary layer and

improved diffusive flux. In contrast, irreversible flow has reduced mass diffusivity due to increased turbulence, which interrupts molecular mobility. Additionally, significantly faster product formation in reversible flow increases energy exchange, which raises the nanofluid temperature due to thermal resistance. Understanding these dynamics is crucial for optimizing heat and mass transfer operations in fields like environmental science and chemical engineering.

Figure 6a highlights the role of mixed convection, where buoyancy and surface stretching jointly affect fluid flow. Stronger mixed convection reduces boundary layer thickness and enhances the velocity profile of the nanofluid. Intensified buoyant effects enhance thermal convection that lowers the temperature profile. It also demonstrates that the velocity of the dusty nanofluid case is lower than that of the pure nanofluid, while the opposite trend is observed for temperature. The decreased velocity is related to higher drag and viscosity caused by the inclusion of dust particles. Additionally, nanoparticles reduce momentum exchange due to the drag force in the dusty phase. The higher temperature in the dusty nanofluid compared to the pure nanofluid is due to dust particles impeding heat dissipation, whereas increased viscosity and drag inhibit convective heat transfer. As the concentration of nanoparticles increases, the temperature of both the dusty and nanofluid phases rises, as shown in Fig. 6b. This is because additional nanoparticles improve thermal conductivity and energy storage capacity. However, higher nanoparticle concentration increases fluid viscosity and reduces fluid mobility, which hinders heat transport and causes thermal buildup. These factors elevate the temperatures of both phases.

These figures reveal that the model involving nanoparticle aggregation reduces the velocity profiles for both the nanofluid and dust phases, while the non-aggregated (homogeneous) model has slightly higher velocities. This behavior is attributed to the agglomeration of nanoparticles into clusters, which increases effective viscosity [48] and internal friction, thereby suppressing fluid flow and momentum transfer in both phases. In contrast, the non-aggregated model maintains lower viscosity and facilitates smoother momentum transfer. From a thermal perspective, aggregation raises temperature profiles due to the formation of thermally conductive clusters, which enhances heat transfer [49,50]. On the other hand, in the homogeneous model, uniformly scattered nanoparticles have limited thermal interaction, resulting in comparatively lower temperatures. Meanwhile, nanoparticle aggregation lowers the concentration profile $\phi(\eta)$ due to the lower number of freely dispersed nanoparticles, which reduces solute availability for diffusion. The streamlines for nanofluid flow in the model with and without nanoparticle aggregation are demonstrated in Fig. 7. The elevated effective viscosity attributed to nanoparticle clusters in the aggregated case produces more resistance to fluid motion, slowing the flow and compressing the streamlines closer to the surface. Plots for skin friction coefficient $C_{f_x} Re_x^{0.5}$ and local Nusselt number $Nu_x Re_x^{0.5}$ for the magnetic parameter, solvent fraction parameter, and aggregation model are presented in Fig. 8. The skin friction indicates the momentum resistance at the boundary, whereas the local Nusselt number characterizes the efficiency of convective heat transfer. As shown in the plot, increasing the magnetic parameter intensifies the Lorentz force, which resists fluid motion and reduces velocity near the surface. This steeper velocity gradient leads to enhanced wall shear stress. The increased Joule heating due to stronger Lorentz force reduces the effective heat transmission. The solvent fraction parameter, which governs the elasticity–viscosity ratio, reduces effective viscosity and strengthens the velocity gradient, thereby increasing the magnitude of $C_{f_x} Re_x^{0.5}$. A larger Λ_1

accelerates fluid motion, reduces the thermal boundary layer, increases the temperature gradient near the surface, and improves heat transmission, thus increasing the Nusselt number. In terms of nanoparticle aggregation, the presence of clustered nanoparticles improves thermal conductivity and facilitates more heat transmission within the boundary layer, resulting in a greater Nusselt number. Simultaneously, aggregation enhances the effective viscosity of the nanofluid, which boosts the velocity gradient close to the boundary and increases the magnitude of skin friction.

7. Conclusion

This article presents a computational investigation of MHD Boger dusty nanofluid flow across a stretching sheet with mixed convection, while considering the significance of reversible reactions. The study evaluates the effective thermophysical properties of nanofluids using aggregation and homogeneous models. Similarity transformations are employed to reduce governing partial differential equations into a system of nonlinear ordinary differential equations. The shooting method is used in conjunction with the Runge-Kutta-Fehlberg (RKF45) technique to solve the transformed system. A systematic parametric study is conducted to investigate the influence of key physical parameters. The notable observations of this analysis are presented as follows:

- Nanofluid flows faster than dusty nanofluid due to added drag and momentum exchange from dust particles.
- Nanoparticle aggregation compresses streamlines and reduces the fluid speed.
- Both dusty and nanofluid phases display increased velocity and temperature with the solvent fraction parameter.
- Both phases' temperatures increase as nanoparticles aggregate, while their velocities decrease.
- An increased magnetic field magnifies the Lorentz force, which heats and decelerates both phases.
- In addition to speeding up the flow, mixed convection raises heat dissipation and lowers temperature.
- The Nusselt number rises as aggregation improves heat transfer by forming enhanced thermal conduction pathways.
- Irreversible flow exhibits lower temperature but higher speed and concentration compared to reversible flows.

The outcomes of this research are directly applicable to various industrial and engineering systems. The stretching sheet configuration models crucial processes such as film production, extrusion, and glass fiber drawing. The viscoelastic Boger fluid represents the behavior of high-performance synthetic polymers, making the study useful in cooling control and die design. Incorporating dust particles enables the simulation of particulate-driven flows relevant to environmental applications such as filtration and pollution management. Aggregation of nanoparticles extends the model's applicability to bioheat transfer, drug delivery systems, and

thermal management in high-density electronics like CPUs, LEDs, and power devices. The esterification process, commonly used in the production of biodiesel, pharmaceuticals, perfumes, and polymers, is also captured in this investigation. Furthermore, magnetic field control provides regulation of heat transfer in temperature-sensitive systems. Overall, this work offers a robust computational foundation for developing adaptable flow control strategies and enhancing heat transfer in both established industrial applications and emerging technological fields.

8. Limitations and future research directions

Limitations

Despite its extensive scope, the applicability is constrained by several assumptions and simplifications. This work is purely theoretical and does not include an experimental component. It considers only laminar, steady, and incompressible flow, while assuming constant thermophysical properties that do not change with temperature or concentration. This model also neglects transient, rotating, and three-dimensional impacts, which may be significant in real-world flow problems. Additionally, the model ignores viscous dissipation and presumes a no-slip interaction between the fluid and dust phases, which could reduce reliability in strong shear or high-temperature environments. Furthermore, relying on approximate numerical methods instead of exact analytical approaches may introduce small but non-negligible errors. Finally, omitting entropy generation analysis limits the understanding of thermal irreversibility and energy efficiency within the system.

Future research directions

Experimental validation remains critical for verifying the theoretical results, particularly for systems involving esterification and aggregation in dusty nanofluids. This framework can be expanded to time-dependent and three-dimensional geometries to better reflect real-world flow scenarios better. Improved nanoparticle modeling, for instance by accounting for non-spherical shapes and size distributions, would increase the understanding of thermal and momentum transport. More sophisticated techniques, such as homotopy analysis or finite element analysis, could further improve solution accuracy and minimize computational errors. The MHD model could also be enriched by incorporating inclined or non-uniform magnetic fields, as well as electro-magneto-hydrodynamic (EMHD) effects. Investigating entropy generation would provide deeper insights into energy efficiency and thermal irreversibility. Future research could potentially relax the no-slip limitation between dust and fluid phases and include viscous dissipation to better describe thermal behavior in strong shear and high-temperature manufacturing processes. Finally, the model's applicability can be broadened by extending it to other non-Newtonian fluid types, such as Carreau, Maxwell, or Casson fluids.

Declarations

Ethical Approval: The authors affirm their commitment to ethical standards.

Conflict of Interest: There is no conflicts of interest to declare.

Author's Contribution: All authors have contributed equally to this work.

Acknowledgment: NA

Data Availability: All the data used during this study is accessible within the manuscript.

References

1. Choi, S.U.S. and Eastman, J.A. "Enhancing thermal conductivity of fluids with nanoparticles", No. ANL/MSD/CP-84938, CONF-951135-29 (Argonne National Lab., IL, 1995). https://www.osti.gov/servlets/purl/196525
2. Malik, M.Y., Naseer, M., Nadeem, S., et al. "The boundary layer flow of Casson nanofluid over a vertical exponentially stretching cylinder", Appl. Nanosci., 4(6), pp. 869–873 (2014). https://doi.org/10.1007/s13204-013-0267-0
3. Ali, B., Ilyas, M., Siddique, I., et al. "Numerical study for bio-convection effects on MHD nano-fluid flow past a porous and extending wedge", Propuls. Power Res., 12(4), pp. 584–594 (2023). https://doi.org/10.1016/j.jppr.2023.11.002
4. Abbas, N., Shatanawi, W. and Taqi, A.M. "Thermodynamic study of radiative chemically reactive flow of induced MHD Sutterby nanofluid over a nonlinear stretching cylinder", Alex. Eng. J., 70, pp. 179–189 (2023). https://doi.org/10.1016/j.aej.2023.02.038
5. Yin, B., Zhang, C., Ding, T., et al. "An experimental and numerical study of gas-liquid two-phase flow moving upward vertically in larger annulus", Eng. Appl. Comput. Fluid Mech., 19(1), 2476605 (2025). https://doi.org/10.1080/19942060.2025.2476605
6. Adhikari, R. and Das, S. "Exploring microbial dynamics in a reactive magnetised Casson-Maxwell-Oldroyd-B nanofluid on a slanted elongated cylinder: Entropy assessment", Int. J. Ambient Energy, 45(1), 2367743 (2024). https://doi.org/10.1080/01430750.2024.2367743
7. Akbar, A.A., Hussain, M., Awan, A.U., et al. "Magnetized heat transfer visualization through computational modeling of third-grade fluid via exponentially stretching cylinder", Mod. Phys. Lett. B, 2450334 (2024). https://doi.org/10.1142/S0217984924503342
8. Khan, A., Ahmad, H., Devi, S.U., et al. "Significance of melting heat transfer in Maxwell nanofluid stagnation point flow across quadratic stratified Riga surface", Results Eng., 104456 (2025). https://doi.org/10.1016/j.rineng.2025.104456
9. Gao, X., Li, Y., Xia, Y., et al. "A review on thermo-fluidic study of droplet impact in spray cooling", Heat Transf. Res., 56(1), pp. 53–91 (2025). https://doi.org/10.1615/HeatTransRes.2024053386
10. Mao, Z., Hosoya, N. and Maeda, S. "Flexible electrohydrodynamic fluid-driven valveless water pump via immiscible interface", Cyborg Bionic Syst., 5, 0091 (2024). https://doi.org/10.34133/cbsystems.0091
11. Murshed, S.M.S., Leong, K.C. and Yang, C. "Enhanced thermal conductivity of TiO_2–water based nanofluids", Int. J. Therm. Sci., 44(4), pp. 367–373 (2005). https://doi.org/10.1016/j.ijthermalsci.2004.12.005
12. Prasher, R., Phelan, P.E. and Bhattacharya, P. "Effect of aggregation kinetics on the thermal conductivity of nanoscale colloidal solutions (nanofluid)", Nano Lett., 6(7), pp. 1529–1534 (2006). https://doi.org/10.1021/nl060992s

13. Daungthongsuk, W. and Wongwises, S. "A critical review of convective heat transfer of nanofluids", Renew. Sustain. Energy Rev., 11(5), pp. 797–817 (2007). https://doi.org/10.1016/j.rser.2005.06.005
14. Liu, M.S., Lin, M.C.C., Tsai, C.Y., et al. "Enhancement of thermal conductivity with Cu for nanofluids using chemical reduction method", Int. J. Heat Mass Transf., 49(17-18), pp. 3028–3033 (2006). https://doi.org/10.1016/j.ijheatmasstransfer.2006.02.012
15. Zhu, H.T., Zhang, C.Y., Tang, Y.M., et al. "Novel synthesis and thermal conductivity of CuO nanofluid", J. Phys. Chem. C, 111(4), pp. 1646–1650 (2007). https://doi.org/10.1021/jp065926t
16. Kumar, R.N., Srilatha, P., Muhammad, T., et al. "Numerical study on nanoparticles aggregation with Brownian motion in fluid flow induced by squeezing porous slider", BioNanoScience, 14(3), pp. 2446–2456 (2024). https://doi.org/10.1007/s12668-024-01367-3
17. Kezzar, M., Ghaffari, A., Dib, A., et al. "MHD nanofluid flow between porous convergent-divergent channel with velocity slip and nanoparticle aggregation", Eng. Sci. Technol. Int. J., 52, 101679 (2024). https://doi.org/10.1016/j.jestch.2024.101679
18. Albalawi, S.K., Karthik, K., Madhu, J., et al. "Nanoparticle aggregation kinematics and nanofluid flow in convectively heated outer stationary and inner stretched coaxial cylinders: Influenced by linear, nonlinear, and quadratic thermal radiation", Mod. Phys. Lett. B, 39(01), 2450361 (2025). https://doi.org/10.1142/S0217984924503615
19. Saffman, P.G. "On the stability of laminar flow of a dusty gas", J. Fluid Mech., 13(1), pp. 120–128 (1962). https://doi.org/10.1017/S0022112062000555
20. Dey, D. and Chutia, B. "Dusty nanofluid flow with bioconvection past a vertical stretching surface", J. King Saud Univ. Eng. Sci., 34(6), pp. 375–380 (2022). https://doi.org/10.1016/j.jksues.2020.11.001
21. Sharif, H., Ali, B., Siddique, I., et al. "Numerical investigation of dusty tri-hybrid Ellis rotating nanofluid flow and thermal transportation over a stretchable Riga plate", Sci. Rep., 13(1), 14272 (2023). https://doi.org/10.1038/s41598-023-43647-0
22. Hussain, M., Ali, B., Awan, A.U., et al. "Role of nanoparticle radius for heat transfer optimization in MHD dusty fluid across stretching sheet", J. Therm. Anal. Calorim., 149(24), pp. 15179–15192 (2024). https://doi.org/10.1007/s10973-024-13738-9
23. Naz, S. "Influence of injection/suction and transient pressure gradient on the Brinkman-type dusty magnetized fluid flow through a horizontal microchannel system", J. Therm. Anal. Calorim., 1–18 (2025). https://doi.org/10.1007/s10973-024-13869-z
24. Boger, D.V. "A highly elastic constant-viscosity fluid", J. Non-Newton. Fluid Mech., 3(1), pp. 87–91 (1977). https://doi.org/10.1016/0377-0257(77)80014-1
25. Ali, B., Siddique, I., Hussain, S., et al. "Boger nanofluid: Significance of Coriolis and Lorentz forces on dynamics of rotating fluid subject to suction/injection via finite element simulation", Sci. Rep., 12(1), 1612 (2022). https://doi.org/10.1038/s41598-022-05487-2
26. Ali, B., Sharif, H., Habib, D., et al. "Significance of tri-hybrid nanoparticles in thermal management subject to magnetized squeezing flow of a Boger-micropolar nanofluid between concentric disks", J. Mol. Liq., 397, 124141 (2024). https://doi.org/10.1016/j.molliq.2024.124141
27. Abbas, M., Khan, N., Hashmi, M.S., et al. "Numerical simulation of chemical reactive flow of Boger fluid over a sheet with heat source and local thermal non-equilibrium

conditions", Case Stud. Therm. Eng., 59, 104498 (2024). https://doi.org/10.1016/j.csite.2024.104498
28. Okasha, M.M., Abbas, M., Norberdiyeva, M., et al. "Characteristics of elastic deformation on Boger hybrid nanofluid using modified Hamilton–Crosser model: A local thermal nonequilibrium model", J. Therm. Anal. Calorim., 1–13 (2025). https://doi.org/10.1007/s10973-024-13919-6
29. Raju, U., Arivukkodi, D., Alhazmi, H., et al. "Heat transfer in a reversible esterification process of hydromagnetic Casson fluid with Arrhenius activation energy", Case Stud. Therm. Eng., 60, 104616 (2024). https://doi.org/10.1016/j.csite.2024.104616
30. Raju, U., Rangabashyam, S., Alhazmi, H., et al. "Irreversible and reversible chemical reaction impacts on convective Maxwell fluid flow over a porous media with activation energy", Case Stud. Therm. Eng., 61, 104821 (2024). https://doi.org/10.1016/j.csite.2024.104821
31. Hussain, M., Awan, A.U., Ali, B., et al. "Characterization of thermal buoyancy forces and suction on bioconvective magnetohydrodynamic dusty nanofluid flow over a stretching surface", Mod. Phys. Lett. B, 2550209 (2025). https://doi.org/10.1142/S0217984925502094
32. Ahmad, B., Ali, B. and Ahmed, M.O. "Numerical simulation for heat optimization via nanofluid in the presence of activation energy: A case of dust particles", Int. J. Thermofluids, 101248 (2025). https://doi.org/10.1016/j.ijft.2025.101248
33. Ali, B., Hussain, S., Nie, Y., et al. "Finite element simulation of bioconvection and Cattaneo-Christov effects on micropolar based nanofluid flow over a vertically stretching sheet", Chin. J. Phys., 68, pp. 654–670 (2020). https://doi.org/10.1016/j.cjph.2020.10.021
34. Awan, A.U., Hussain, M., Ali, B., et al. "Computational analysis of entropy generation in EMHD micropolar dusty fluid flow incorporating esterification process", Sci. Rep., 15, 30146 (2025). https://doi.org/10.1038/s41598-025-15017-5
35. Wang, J., Mustafa, Z., Siddique, I., et al. "Computational analysis for bioconvection of microorganisms in Prandtl nanofluid Darcy–Forchheimer flow across an inclined sheet", Nanomaterials, 12(11), 1791 (2022). https://doi.org/10.3390/nano12111791
36. Aljerf, L. and Nadra, R. "Developed greener method based on MW implementation in manufacturing CNFs", Int. J. Nanomanuf., 15(3), pp. 269–289 (2019). https://doi.org/10.1504/IJNM.2019.100461
37. Ellahi, R., Hassan, M. and Zeeshan, A. "Aggregation effects on water base Al_2O_3—nanofluid over permeable wedge in mixed convection", Asia-Pac. J. Chem. Eng., 11(2), pp. 179–186 (2016). https://doi.org/10.1002/apj.1954
38. Mahanthesh, B. and Thriveni, K. "Nanoparticle aggregation effects on radiative heat transport of nanoliquid over a vertical cylinder with sensitivity analysis", Appl. Math. Mech., 42, pp. 331–346 (2021). https://doi.org/10.1007/s10483-021-2687-7
39. Ali, B., Siddique, I., Ahmad, H., et al. "Influence of nanoparticles aggregation and Lorentz force on the dynamics of water-titanium dioxide nanoparticles on a rotating surface using finite element simulation", Sci. Rep., 13(1), 4702 (2023). https://doi.org/10.1038/s41598-023-33068-4
40. Rashid, S., Hayat, T., Qayyum, S., et al. "Three-dimensional rotating Darcy–Forchheimer flow with activation energy", Int. J. Numer. Methods Heat Fluid Flow, 29(3), pp. 935–948 (2019). https://doi.org/10.1108/HFF-06-2018-0292

41. Sarlo, E., Svoronos, P. and Kulas, P. "Calculation of equilibrium constant in esterification reactions", J. Chem. Educ., 67(9), p. 796 (1990). https://doi.org/10.1021/ed067p796
42. Ramesh, G.K., Gireesha, B.J. and Bagewadi, C.S. "Heat transfer in MHD dusty boundary layer flow over an inclined stretching sheet with non-uniform heat source/sink", Adv. Math. Phys., 2012, 657805 (2012). https://doi.org/10.1155/2012/657805
43. Jalil, M., Asghar, S. and Yasmeen, S. "An exact solution of MHD boundary layer flow of dusty fluid over a stretching surface", Math. Probl. Eng., 2017, 2307469 (2017). https://doi.org/10.1155/2017/2307469
44. Wang, C.Y. "Free convection on a vertical stretching surface", ZAMM-J. Appl. Math. Mech., 69(11), pp. 418–420 (1989). https://doi.org/10.1002/zamm.19890691115
45. Khan, W.A. and Pop, I. "Boundary layer flow of a nanofluid past a stretching sheet", Int. J. Heat Mass Transf., 53(11-12), pp. 2477–2483 (2010). https://doi.org/10.1016/j.ijheatmasstransfer.2010.01.032
46. Ding, M., Tang, M., Hua, Z., et al. "Magnetic field sensing by magnetic-fluid-coated capillary long-period fiber gratings", J. Opt. Photonics Res., 1, pp. 124–130 (2024). https://doi.org/10.47852/bonviewJOPR32021778
47. Wang, H., He, Q., Yuan, S., et al. "Magnetic field sensor using the magnetic fluid-encapsulated long-period fiber grating inscribed in the thin-cladding fiber", J. Opt. Photonics Res., 1, pp. 210–215 (2025). https://doi.org/10.47852/bonviewJOPR32021689
48. Gharagozloo, P.E. and Goodson, K.E. "Temperature-dependent aggregation and diffusion in nanofluids", Int. J. Heat Mass Transf., 54(4), pp. 797–806 (2011). https://doi.org/10.1016/j.ijheatmasstransfer.2010.06.058
49. Wei, W., Cai, J., Hu, X., et al. "Fractal analysis of the effect of particle aggregation distribution on thermal conductivity of nanofluids", Phys. Lett. A, 380(37), pp. 2953–2956 (2016). https://doi.org/10.1016/j.physleta.2016.07.005
50. Chen, H., Witharana, S., Jin, Y., et al. "Predicting thermal conductivity of liquid suspensions of nanoparticles (nanofluids) based on rheology", Particuology, 7(2), pp. 151–157 (2009). https://doi.org/10.1016/j.partic.2009.01.005

Biography

Muzammil Hussain is pursuing his Ph.D. in Mathematics at the University of the Punjab, Lahore. He serves as a Lecturer in Mathematics at the Higher Education Department, Punjab, Pakistan, after securing the top merit position in the Punjab Public Service Commission in 2022. He earned distinction by securing first position in BS Mathematics at the University of Sargodha. His research expertise lies in computational analysis of heat transfer in multiphase fluid flows.

Dr. Aziz Ullah Awan has been working as a tenured Professor at the Institute of Mathematics, University of the Punjab, Lahore, Pakistan. He is working in the field of

Fluid Dynamics; Bio-mathematics and Soliton theory. He completed his Ph.D. in 2012 from ASSMS, GC University Lahore, Pakistan.

List of Figure and Table Captions

Figures and Tables

Table 1: Distinction of current study from existing literature.

Authors	Boger Fluid	Dusty Fluid	Nanofluid	Aggregation	Esterification	Buoyancy Effects	Stretching Sheet
Abbas et al. [27]	Yes	No	No	No	No	No	Yes
Raju et al. [29]	No	No	No	No	Yes	Yes	Yes
Raju et al. [30]	No	No	No	No	Yes	No	Yes
Ali et al. [26]	Yes	No	Yes	No	No	No	No

Okasha et al. [28]	Yes	Yes	Yes	No	No	No	No
Hussain et al. [31]	No	Yes	Yes	No	No	Yes	Yes
Ahmad et al. [32]	No	Yes	Yes	No	No	Yes	Yes
Current study	**Yes**	**Yes**	**Yes**	**Yes**	**Yes**	**Yes**	**Yes**

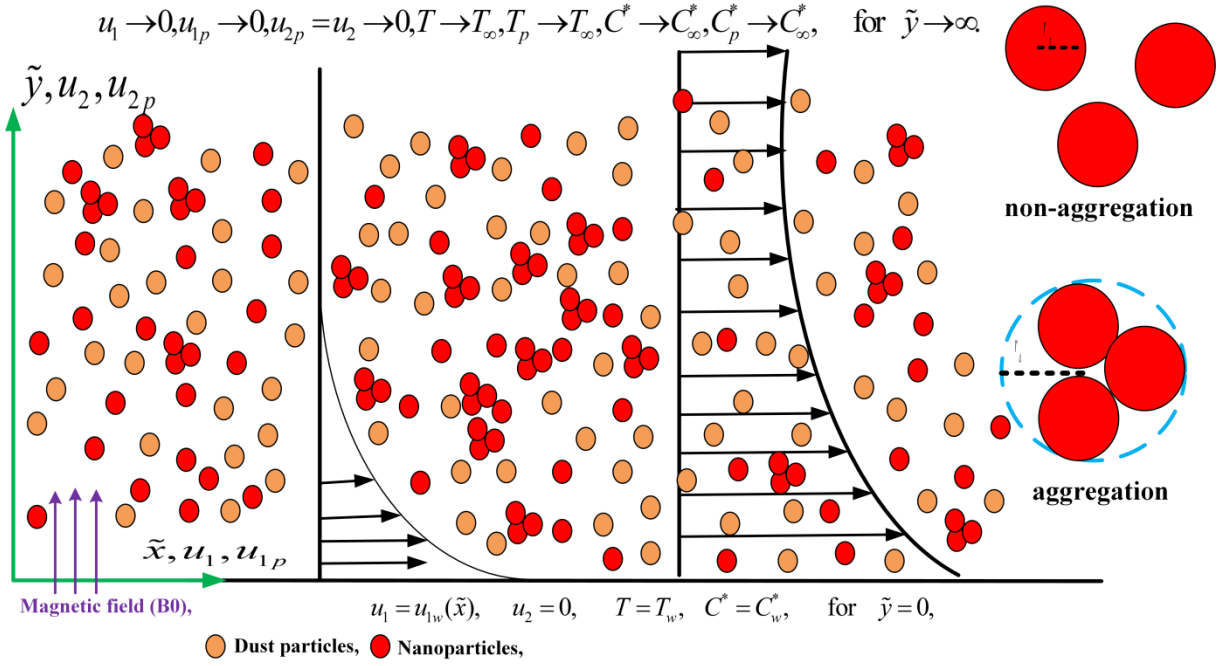

Fig. 1: Geometry of the problem.

Table 2: Comparison of thermo-physical characteristics with and without nanoparticle aggregation.

Properties	With nanoparticle aggregation	Without nanoparticle aggregation
Density	$\rho_{nf} = (1-\Phi_{agr})\rho_f + \Phi_{agr}\rho_s$	$\rho_{nf} = (1-\Phi)\rho_f + \rho_s\Phi$
Viscosity	$\mu_{nf} = \mu_f \left(1-\frac{\Phi_{agr}}{\Phi_{max}}\right)^{-2.5\Phi_{max}}$	$\mu_{nf} = \frac{\mu_f}{(1-\Phi)^{2.5}}$
Thermal Conductivity	$k_{nf} = k_f \left(\frac{k_{agr}+2(k_{agr}-k_f)\Phi_{agr}+2k_f}{k_{agr}-(k_{agr}-k_f)\Phi_{agr}+2k_f}\right)$	$k_{nf} = k_f \left(\frac{k_s+2(k_s-k_f)\Phi+2k_f}{k_s+(k_f-k_s)\Phi+2k_f}\right)$
Heat Capacity	$(\rho c_p)_{nf} = (1-\Phi_{agr})(\rho c_p)_f + (\rho c_p)_s\Phi_{agr}$	$(\rho c_p)_{nf} = (1-\Phi)(\rho c_p)_f + (\rho c_p)_s\Phi$

Table 3: Physical interpretation of dimensionless parameters.

Symbol	Name	Physical interpretation
N_r	Buoyancy ratio parameter	Compares the contributions of solutal and thermal buoyancy forces
λ_θ	Thermal buoyancy parameter	Highlights thermal effects in buoyancy-induced fluid flow
Pr	Prandtl number	Accounts for the balance between momentum and thermal diffusivity
M	Magnetic parameter	Measures influence of Lorentz force due to applied magnetic field
S_c	Schmidt number	Ratio of momentum diffusivity to mass diffusivity
γ_t	Thermal relaxation parameter	Captures thermal lag between fluid and dust phases
Γ_v	Momentum coupling parameter	Quantifies interphase momentum transfer
β_t	Thermal interaction parameter	Measures the strength of thermal coupling between both phases
β_c	Concentration interaction parameter	Governs solute exchange between both phases
β_v	Velocity interaction parameter	Represents drag due to relative motion between fluid and dust

Table 4: Comparison of skin friction coefficients for varying M and β_v, and neglecting other parameters, with results from Ramesh et al. [42], Jalil et al. [43], and Hussain et al. [22].

M	$\beta_v = 0$				$\beta_v = 0.5$		
	Ramesh et al. [42]	Jalil et al.[43]	Hussain et al. [22]	Current Results	Jalil et al. [43]	Hussain et al. [22]	Current Results
0.2	1.095	1.095445	1.09540	1.09528	1.126114	1.1263	1.12614
0.5	1.224	1.224745	1.22470	1.22448	1.252251	1.2524	1.25222

1.0	1.414	1.414214	1.41420	1.41414	1.438101	1.4381	1.43807
1.5	1.581	1.581139	1.58850	1.58255	1.602540	1.6025	1.60235
2.0	1.732	1.732051	1.73200	1.73202	1.751609	1.7517	1.75144

Table 5: Comparison of Nusselt number for varying Prandtl number and neglecting other parameters, with results from Wang [44], Khan and Pop [45], and Hussain et al. [31].

Pr	Wang [44]	Khan and Pop [45]	Hussain et al. [31]	Current Results
0.7	0.4539	0.4539	0.4541736	0.453736
2.0	0.9114	0.9113	0.911326	0.911226
7.0	1.8954	1.8954	1.895400	1.895440
20	3.3539	3.3539	3.353901	3.3538801

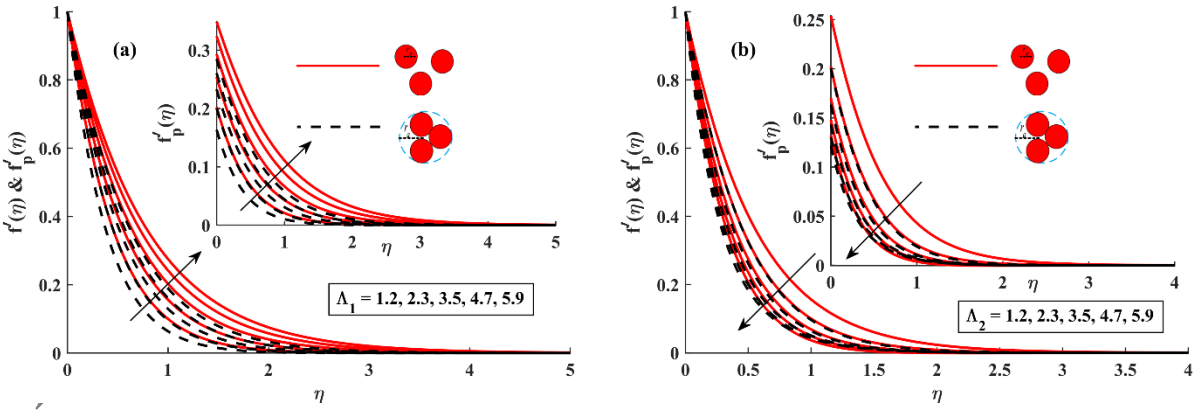

Fig. 2: Influence of varying Λ_1 and Λ_2 on velocity profiles.

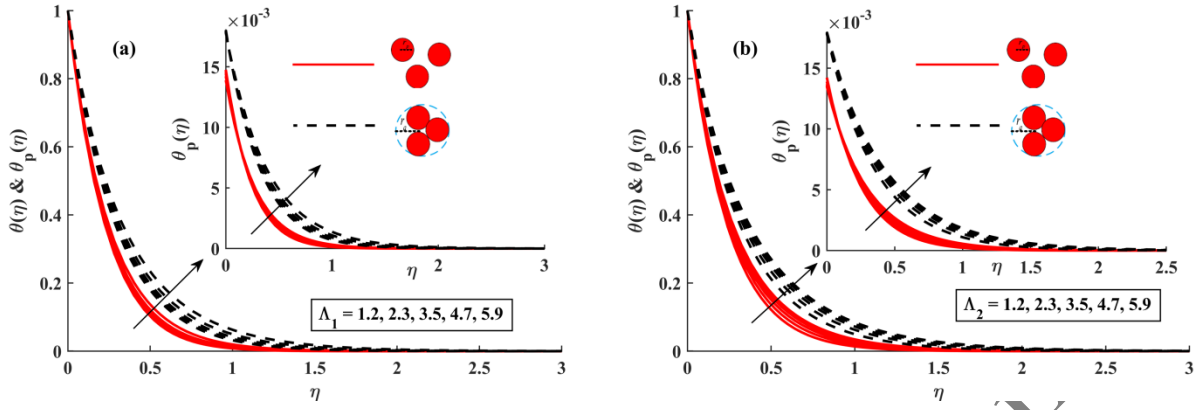

Fig. 3: Influence of varying Λ_1 and Λ_2 on temperature profiles.

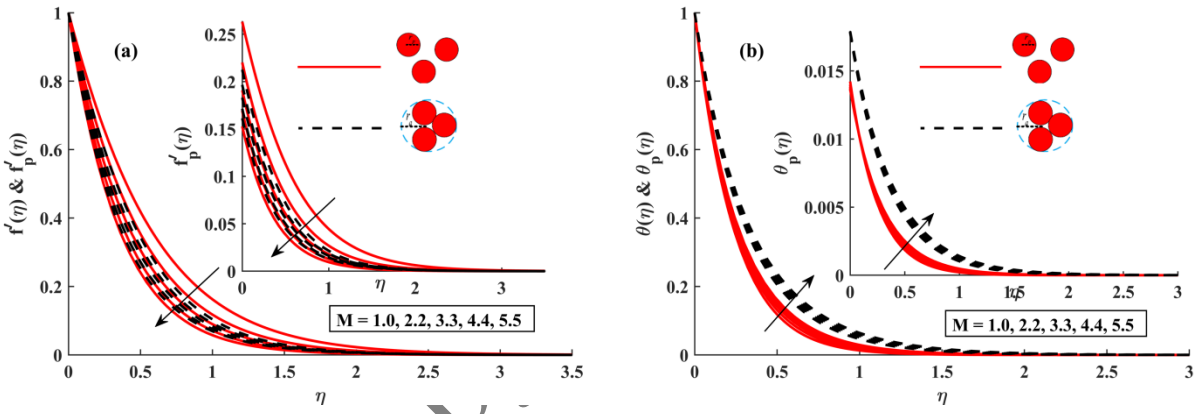

Fig. 4: Influence of varying M on velocity and temperature profiles.

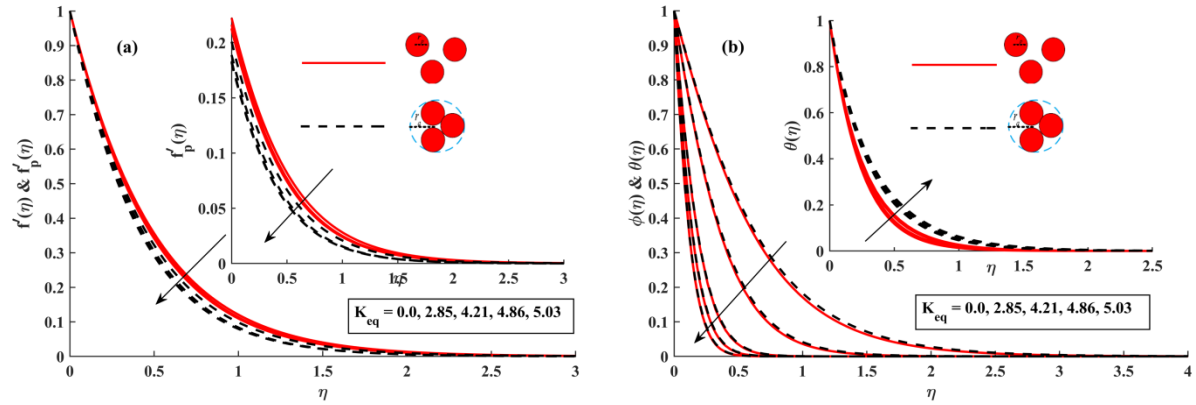

Fig. 5: Influence of varying K_{eq} on velocity, temperature, and concentration profiles.

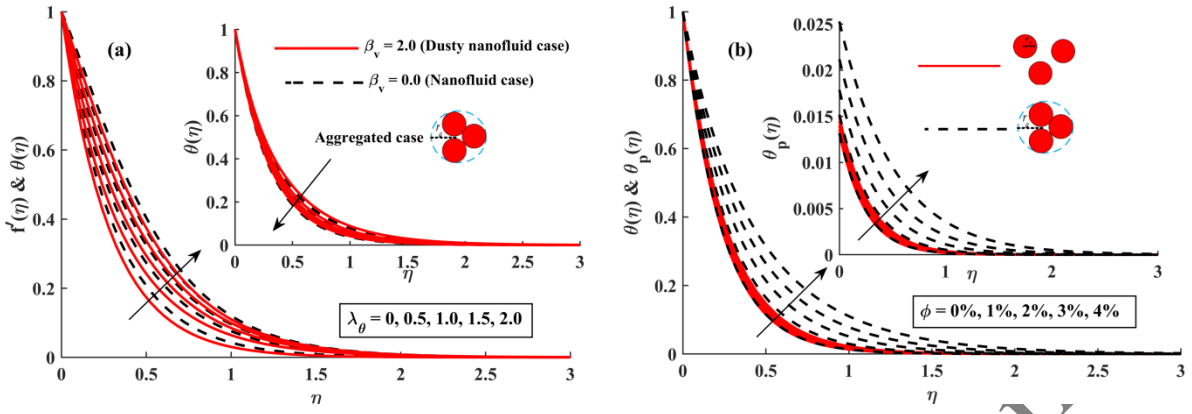

Fig. 6: Influence of varying λ_θ and ϕ on velocity and temperature profiles.

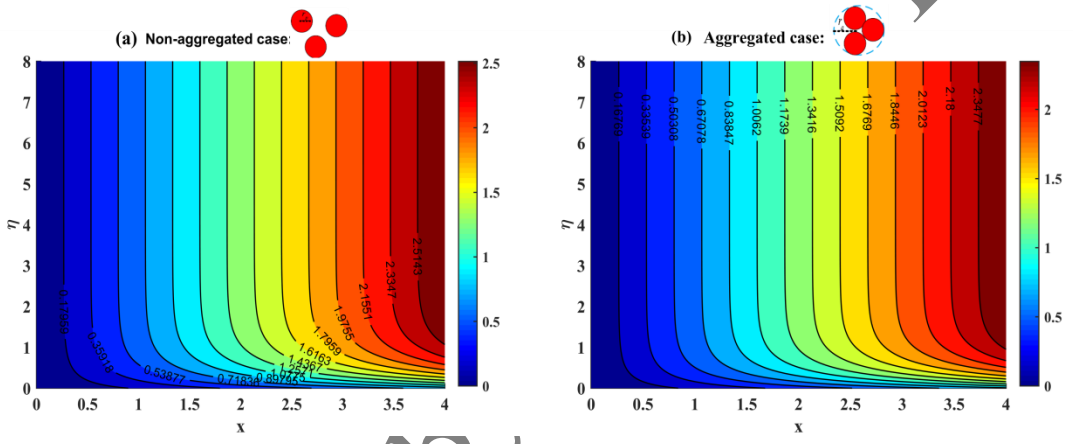

Fig. 7: Streamlines for aggregated and non-aggregated cases.

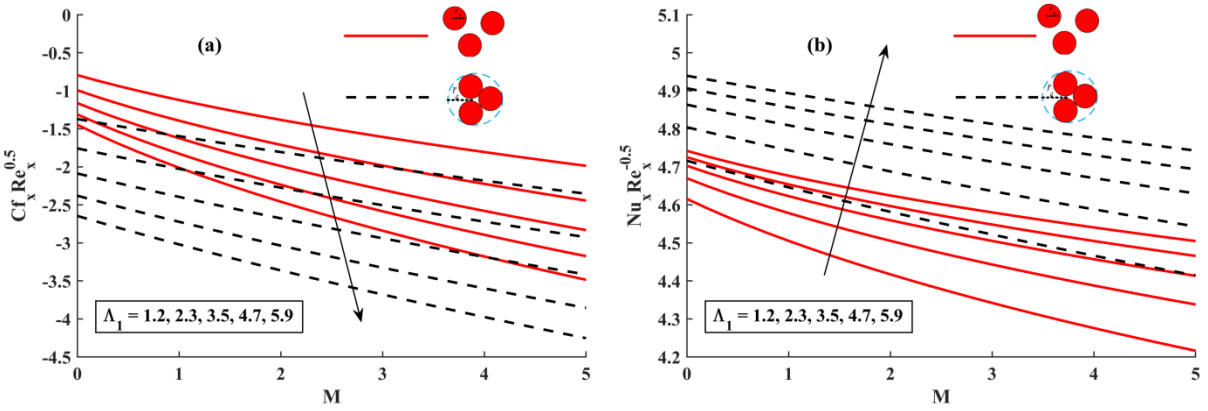

Fig. 8: Influence of varying M and Λ_1 on skin friction and Nusselt number.

Nomenclature

ν_{nf}	Kinematic viscosity of the nanofluid	ρ_{nf}	Density of the nanofluid
$K = 6\pi\mu r$	Stokes' drag constant	B_0	Strength of the uniform magnetic field
σ_{nf}	Electrical conductivity of the nanofluid	τ_T	Thermal equilibrium time
c_p	Specific heat capacity of the fluid	c_m	Specific heat capacity of dust particles
(u_{1p}, u_{2p})	Velocity components of the dust phase	(u_1, u_2)	Velocity components of the fluid phase
Λ_1	Solvent fraction parameter	Λ_2	Relaxation time ratio
M	Magnetic field parameter	β_c	Concentration-phase interaction parameter
β_t	Temperature-phase interaction parameter	γ_t	Specific heat ratio
β_v	Velocity-phase interaction parameter	Pr	Prandtl number
$\tilde{g}_1$	Gravitational acceleration	u_{1w}	Stretching velocity of the sheet
C_{f_x}	Skin friction coefficient	Nu_x	Local Nusselt number
Sh_x	Local Sherwood number	D_B	Brownian diffusion coefficient
λ_θ	Mixed convection parameter	S_c	Schmidt number
N_r	Buoyancy ratio parameter	K_{eq}	Chemical equilibrium constant